CONSTITUTIVE AND FRACTURE TOUGHNESS PROPERTIES OF AN ADVANCED FERRITIC/ MARTENSITIC STEEL — P. Spätig, G. R. Odette, G. E. Lucas and M. Victoria (University of California, Santa Barbara); M. Victoria (Technologie de la Fusion–Centre de Recherches en Physique des Plasmas, Ecole Polytechnique Fédérale de Lausanne)

OBJECTIVE

The objectives of this work are to characterize both the constitutive and fracture behavior of advanced ferritic-martensitic steels in support of developing physically based models for accurately predicting defect tolerance in flawed fusion structures, based, in large part, on small specimen test methods. This report focuses on developing a compact, multi-term constitutive equation for the IEA heat of martensitic steel, with special emphasis on strain-hardening behavior. New effective fracture toughness-temperature data are also presented, along with an update on the status of the US-Swiss collaborative Master Curve Experiment (MACE).

SUMMARY

A detailed investigation of the strain-hardening rate of the International Energy Agency (IEA) program heat of 8 Cr unirradiated F82H ferritic-martensitic steel has been undertaken in the temperature range [80K-723K]. The overall tensile flow stress is decomposed into an athermal/ thermal yield stress contribution plus a mildly temperature-dependent strain-hardening component. The latter is based on a phenomenological dislocation mechanics model. Compared to simple power law treatments, this formulation provides a more accurate and physically based representation of the flow stress as a function of the key variables of test temperature, strain and stain rate. Fracture toughness measurements from small 0.18T CT specimens are also reported and analyzed using a constraint correction model to estimate a small scale yielding $K_{Ic}(T)$ toughness curve. Finally, the status of the MACE collaboration is briefly summarized. The first irradiation at 250°C to 0.5 dpa has been tentatively completed, and is awaiting confirmation of the preliminary dosimetry. Near term plans for higher doses and other temperatures are described.

PROGRESS AND STATUS

Materials and testing conditions

The alloy investigated in this study was the modified, normalized and tempered martensitic steel F82H. This is the reduced activation steel internationally investigated as part of the IEA coordinated program on ferritic/martensitic steels. The heat-treatment of this steel was:

- 0.5h at 1313K for normalization and 2h at 1013K for tempering

Tensile tests ware performed on round specimens (3mm diameter, 18 mm gauge length). The tests were carried out with a servo-hydraulic MTS machine at constant nominal strain rate of $2x10^{-4}$ s^{-1}, $2x10^{-3}$ s^{-1} and $2x10^{-2}$ s^{-1}. Tests at higher temperature (up to 723K), performed at the Paul Scherrer Institute in Switzerland at constant nominal strain rate of $2.8x10^{-5}$ s^{-1} and $2.8x10^{-4}s^{-1}$, are also reported and reanalysed in this report.

The fracture toughness tests were performed on 20% side-grooved 0.18T CT specimens using procedures described elsewhere [1].

Tensile testing

Two typical true stress-true strain curves at 293K and 123K are presented on Figure 1. The two curves look quite similar with a strain-hardening rate, defined as $\theta_p = d\sigma/d\varepsilon_p$, decreasing along the entire curve. The "parabolic" type of curve seen on Figure 1 has been found at all temperatures and strain rates. Prior to necking, a roughly similar amount of strain hardening is observed in both cases. However, there are important and subtle differences as well. For example, near the yield stress $\sigma_{0.2}$, defined at 0.2% plastic strain, the transition between the elastic and the plastic domain is very smooth at 293K, while at 123K a pronounced slope change is observed. Other systematic effects of temperature on hardening at higher strains are not negligible and are analyzed below.

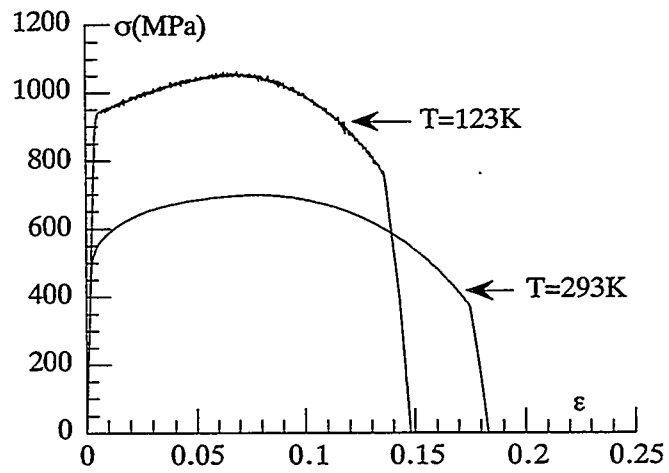

Figure 1: True stress - true strain tensile curve at 293K and 123K.

Understanding of the strain-hardening requires a flow stress decomposition into several contributions. The overall flow stress, which depends on the plastic strain, plastic strain rate and temperature $\sigma=\sigma(\varepsilon_p, \dot{\varepsilon}_p, T)$ can be considered as the sum of the yield stress, σ_y, and the contribution from plastic deformation σ_{pl}, primarily resulting from dislocation-dislocation interactions. It was previously shown [2] that σ_y exhibits a strong temperature and strain rate dependence, as expected for bcc materials. The strain hardening contribution is expected to be much less sensitive to temperature and strain rate. A reasonable general trial decomposition of the flow stress is:

$$\sigma = \sigma_y(\dot{\varepsilon}_p, T) + \sigma_{pl}(\varepsilon_p, \dot{\varepsilon}_p, T) \qquad (1)$$

The σ_y term can itself be decomposed into different athermal and thermal components due to both the lattice friction stress and microstructure resulting from the alloy composition and thermal-mechanical treatment, including contributions from:

- the initial dislocation density
- the distribution of nondeforming particles such as carbides

- the distribution of weaker precipitate phases
- the solid solution hardening
- polycrystalline grain and subgrain boundaries
- the intrinsic friction stress of the lattice (Peierls stress) which is primarily responsible for the strong temperature and strain rate dependence.

The increase of σ_{pl} with strain, i.e. the strain-hardening $\theta_p = d\sigma_{pl}/d\varepsilon_p$, is primarily determined by the evolution of the dislocation microstructure in the material. Both the variation of the total dislocation density with strain and the organization of dislocations into a substructure determine the shape of the deformation curve. A convenient way of presenting the evolutionary behavior of the constitutive behavior of metals, as proposed by Mecking [3], is plotting θ_p, evaluated from the experimental tensile curves between yield and necking, against the corresponding flow stress.

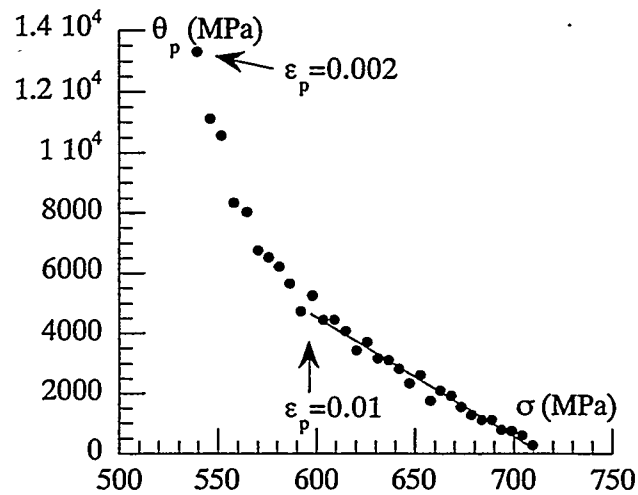

Figure 2: Strain-hardening rate θ_p vs. flow stress at T=273K.

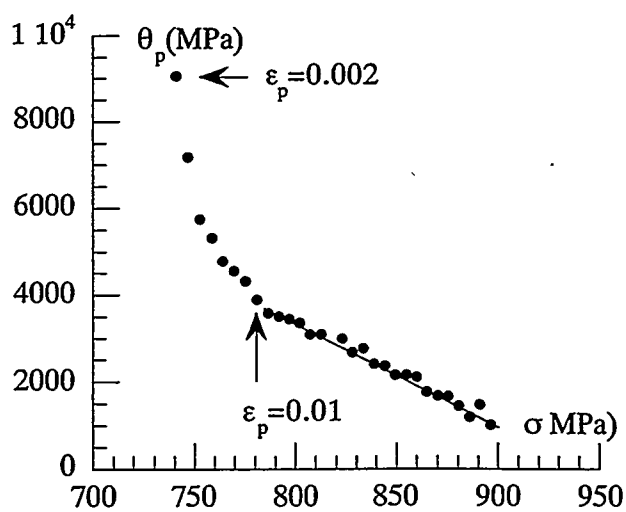

Figure 3: Strain-hardening rate θ_p vs. flow stress at T=173K.

This procedure is not only very useful in establishing appropriate analytical relations for integrated stress-strain laws, $\sigma_{pl}(\varepsilon_p)$, but also in identifying various strain-hardening stages associated with different mechanism regimes. Figures 2 and 3 show θ_p versus the flow stress between ε_p=0.002 and necking at 273K and 173K respectively. In both cases there appears to be a simple linear relation between θ_p and σ_{pl} at high stress. However below a stress, corresponding to $\varepsilon_p \approx 0.01$, θ_p deviates from the simple linear relation, rising increasingly rapidly with decreasing σ_{pl}.

θ_p for plastic strain larger than $\varepsilon_p > 0.01$ can be simply written as:

$$\theta_p = \frac{d\sigma_{pl}}{d\varepsilon_p} = K_1(\dot{\varepsilon}_p, T) - K_2(\dot{\varepsilon}_p, T)(\sigma - \sigma_{0.01}) \qquad (2)$$

where the coefficient K_1 and K_2 are in MPa and dimensionless, respectively. Note an explicit strain rate and temperature dependence on the coefficient K_1 and K_2 have been retained. Integration of Equation 2 with the initial condition $\sigma = \sigma_{0.01}$ at $\varepsilon_p = 0.01$ yields:

$$\sigma_{pl}(\varepsilon_p) = \frac{K_1}{K_2}[1 - \exp[-K_2[\varepsilon_p - 0.01]]] + \sigma_{0.01} \qquad (3)$$

However, it is more convenient to write Equation 3 as,

$$\sigma_{pl}(\varepsilon_p) = \sigma_{sat} - \frac{K_1}{K_2}\exp[-K_2[\varepsilon_p - 0.01]] \qquad (4)$$

where the saturation stress, σ_{sat}, is equal to $K_1/K_2 + \sigma_{0.01}$. The exponential type of stress-strain relation was originally proposed, accompanied by a mechanistic justification, by Voce [4]. The temperature and strain rate dependence of σ_{pl}, if any, is contained in the K_1, K_2 and σ_{sat} terms. This relation describes the behavior of stress-strain curves tending to a saturation stress, which typically cannot be reached in a tensile test due to necking, nominally at $\theta_p=\sigma$. Note that the classical strain-hardening law for engineering materials of the type $\sigma=K\varepsilon_p^n$, would provide a poor fit to this experimental data, since this representation is not compatible with a linear decrease of θ_p or with a σ_{sat}. Further, n implicitly depends on σ_y and a higher σ_y requires a lower n even if the actual strain hardening behavior were completely athermal. Figure 4 shows the fit to Equation 3 of experimental data at 173K. Similar quality fits at other temperatures were also obtained.

Following the work of Kocks [5] for copper, aluminum and stainless steel, plots of non-dimensional σ_{sat}/μ and $(K_1/K_2)/\mu$ are presented on Figure 5 and Figure 6 respectively as a function of the dimensionless temperature, $100kT/\mu b^3$. Here μ is the shear modulus and b is the Burgers vector. The temperature dependence of μ was deduced from that of the Young's modulus [6]; and b was taken equal to 2.68 Å. The logarithms of both σ_{sat}/μ and $(K_1/K_2)/\mu$ decrease roughly linearly with $100kT/\mu b^3$ between values of about 0.2 to 0.76, corresponding to T=223K and 723K. The temperature dependence of K_2 is given on Figure 7 where it is seen that K_2 increases roughly linearly with normalized temperature between about 0.2 and 0.63, corresponding to 223K and 623K.

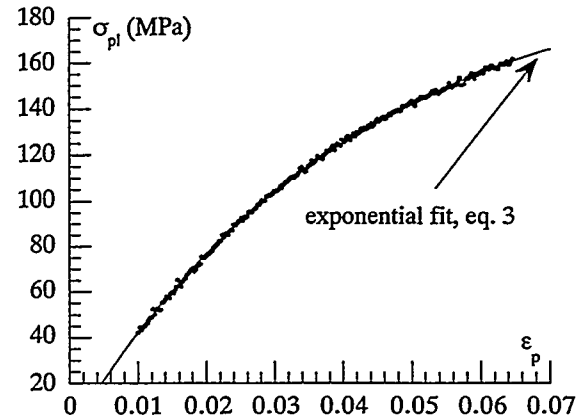

Figure 4: σ_{pl} vs ε_p at 173K with the exponential fit, eq. (4).

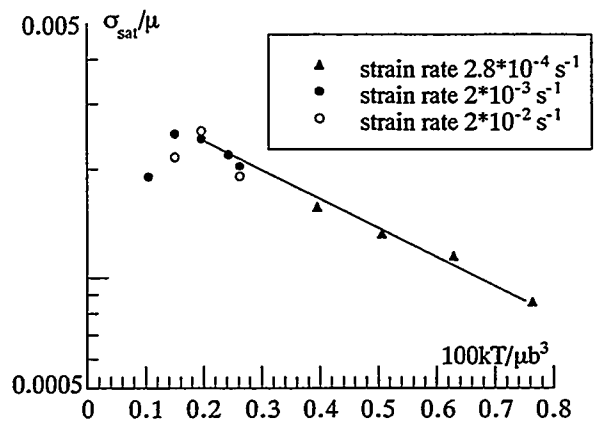

Figure 5: Normalized σ_{sat} against normalized temperature

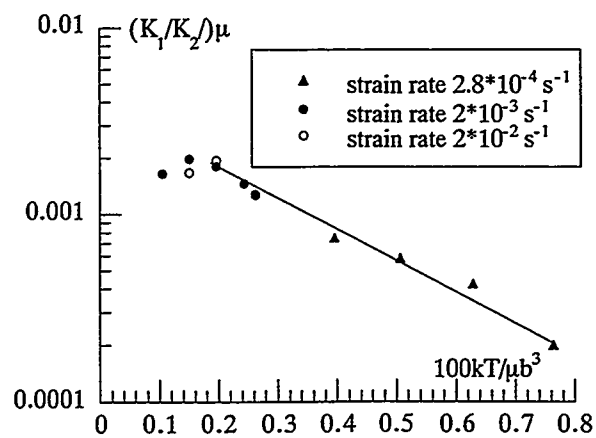

Figure 6: Normalized K_1/K_2 against normalized temperature

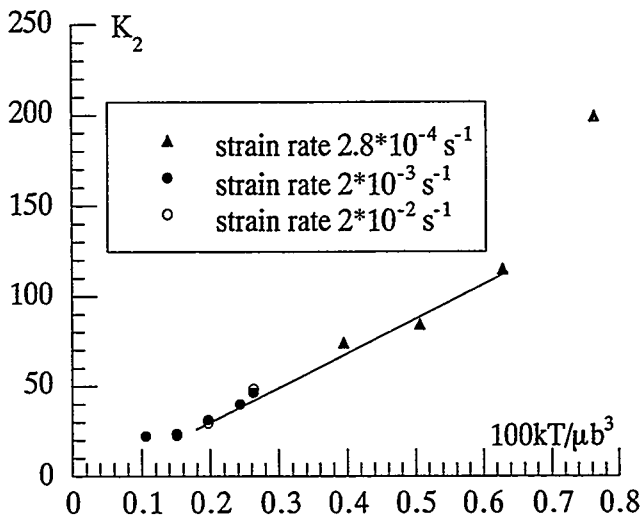

Figure 7: K_2 against normalized temperature

There is no evidence of a strain rate dependence of $(K_1/K_2)/\mu$, σ_{sat}/μ or K_2 for the limited strain rate range in this study. Least square fits to the data from 223K-623K, shown as the solid line in Figures 5, 6 and 7, are:

$$(K_1 / K_2) / \mu = 33.501 * 10^{-4} * (3.232 * 10^{-2})\hat{}\, x \qquad (5a)$$

$$\sigma_{sat} / \mu = 33.174 * 10^{-4} * (1.705 * 10^{-1})\hat{}\, x \qquad (5b)$$

$$K_2 = -4.1087 + 186.86 * x \qquad (5c)$$

with $x = 100kT/mb^3$ for $0.2 < x < 0.63$ and $m=E/2(1+n)$ where n is the Poisson's ratio and $E=6900*(32.3-6.16*10^{-3}T-4.34*10^{-6}T^2)$ for E in MPa and T in °K.

Figure 8 plots the absolute magnitude of the saturation stress versus temperature along with $s_{0.2}$ at the strain rate of $2x10^{-3}$ s^{-1}. The total flow stress is simply the sum of these two individually aggregated contributions. However, $s_{0.2}$ depends strongly on the strain rate as well as temperature. The temperature T for a strain rate $\dot{\varepsilon}$ different than a reference strain rate $\dot{\varepsilon}_r$ at T' for the same $s_{0.2}$ is given by the relation:

$$T' = T[1 + C\ln(\dot{\varepsilon}_r / \dot{\varepsilon})] \qquad (6)$$

Figure 9 shows yield stress, $\sigma_{0.2}/\mu$ versus a strain-rate compensated temperature, T', for a reference strain rate of $2x10^{-4}$ s^{-1}. The solid line is for C =0.0417, which is somewhat larger than found previously [6]. In this case C was derived for the temperature dependent regime I below about 220°K, $\sigma_{0.2}/\mu$ corresponds to an athermal plus activated flow process. In regime I the controlling mechanism is of Peierls type, where $\dot{\varepsilon}_p = \dot{\varepsilon}_o \exp(-\Delta G / kT)$, and where $\Delta G \approx kT/C$ [2].

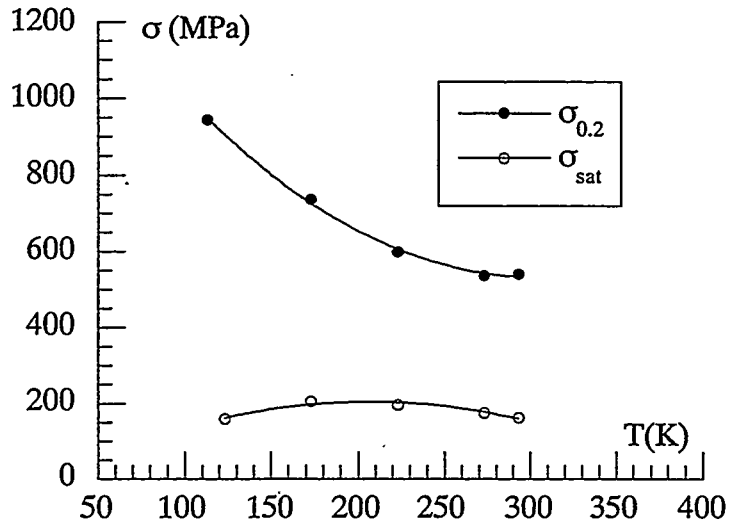

Figure 8: $\sigma_{0.2}$ and σ_{sat} against T for $\dot{\varepsilon}_p = 2\times10^{-3}\ s^{-1}$

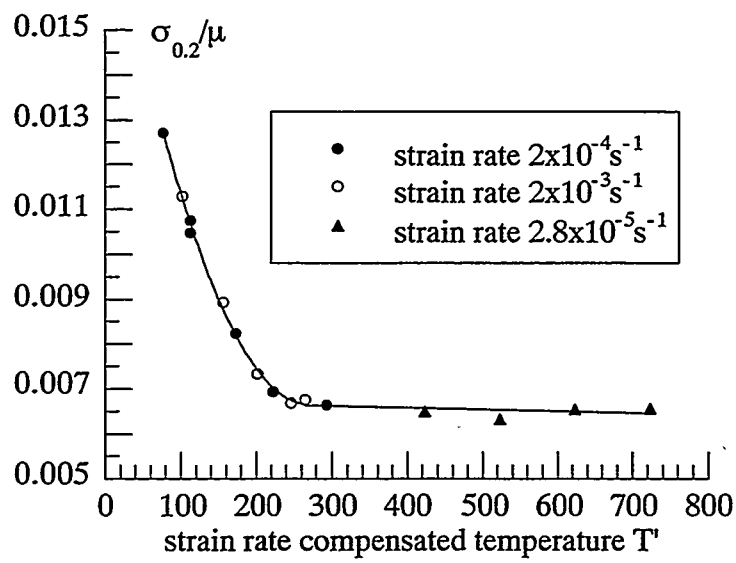

Figure 9: Strain rate compensated temperature dependence of the normalized yield stress

In the temperature regime II from about 220K to 300K the yield stress is more weakly thermally activated and approximately athermal in regime III above 300K. In the latter temperature regime, the plastic flow is considered to be controlled by polycrystalline grain and lath packet sizes, long range stresses, discrete dislocation obstacles and interactions between the moving and the forest dislocations like in the FCC materials. The overall temperature dependence of $\sigma_{0.2}$ is given by:

$$\sigma_{0.2} / \mu = 67.49 * 10^{-4} - 3.90 * 10^{-7} * T' \qquad 270K<T'<723K \quad (7a)$$

$$\sigma_{0.2} / \mu = 18.51 * 10^{-3} - 87.61 * 10^{-6} * T' + 16.17 * 10^{-8} * T'^{2} \qquad T'<270K \quad (7b)$$

An example of application of equations 5 to 7 is shown on Figure 10 where the measured flow stress of several tensile tests is plotted against the calculated flow stress. The flow stresses have been calculated between the yield stress $\sigma_{0.2}$ and the stress at necking at different strain levels for tests at temperatures ranging from 223K to 623K and for strain rates between $2x10^{-4}s^{-1}$ and $2.8x10^{-5}s^{-1}$. Each symbol corresponds to a test at a given temperature and strain rate. A very good agreement between the calculated stresses and the experimental data is found and the model predicts the data within an error margin of less than 4%.

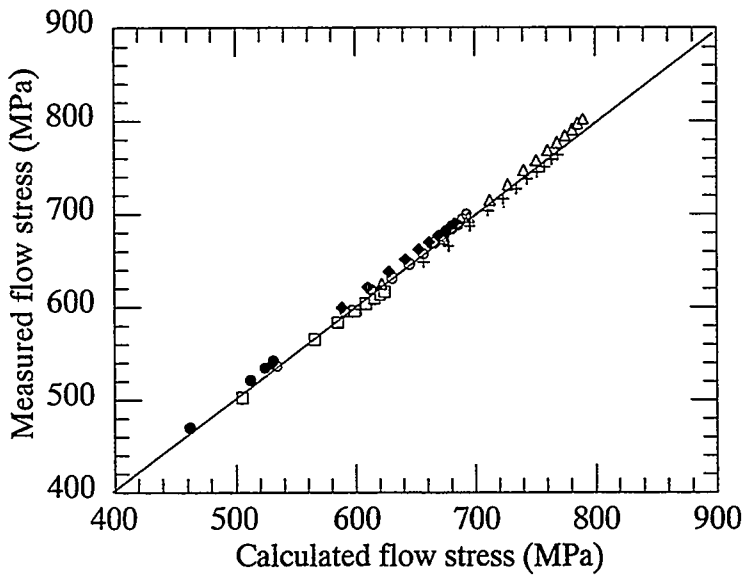

Figure 10: Measured flow stress vs. calculated flow stress for different temperatures and strain rates.

The reversibility of the flow stress has been tested with Cottrell-Stokes experiments [7]. This type of experiment is performed in two steps. First, one specimen is deformed up to a given strain at a fixed temperature T_1 and unloaded. Then, the test temperature is changed to T_2 and the deformation is continued. Usually T_2 is chosen lower than T_1 in order to avoid irreversible annealing processes. The flow stress required to deform plastically the specimen at T_2 can be compared to that obtained on a specimen tested only at T_2. This technique allows one to quantify the influence of temperature on the development of the microstructure and to assess the reversibility of the flow stress for a given strain-hardened state. An example of a Cottrell-Stokes experiment is shown in Figure 11 for which a specimen of the IEA steel has been deformed up to about 0.02 plastic strain and than deformed at a lower temperature. The second deformation curve at T_2 is compared to that of a single reference specimen tested only at T_2. The pre-deformation up to 0.02 plastic strain at T_1 does not influence the flow stress and/or the strain-hardening for deformation at T_2. Similar experiments performed between the temperatures T_1-T_2 equal to 293K-223K and 223K-123K showed no influence of pre-deformation. Thus, while the strain-hardening rate has been found slightly temperature sensitive, the flow stress appears to depend only on the existing deformation. This observation provides additional support to the conclusion that the temperature dependence of the strain-hardening is weak.

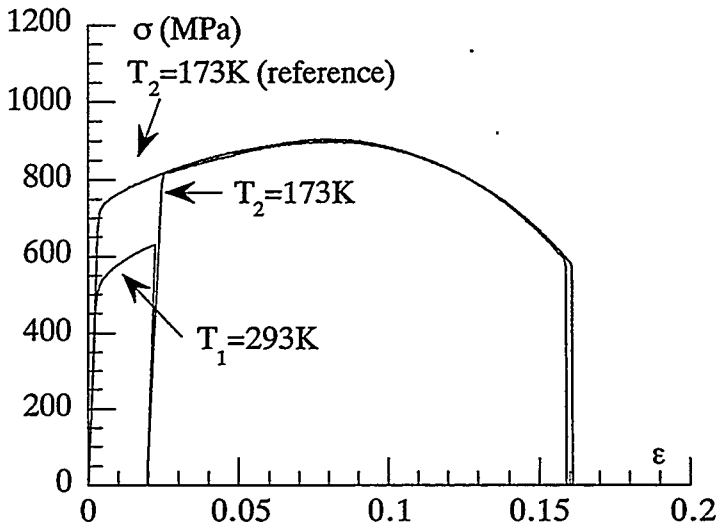

Figure 11: Cottrell-Stokes experiment between T_1=293K and T_2=173K, IEA steel

The strain-hardening law presented above is semi-empirical and the physical meaning of the parameters, K_1 and K_2, is not obvious, especially for a physical system as complex as a ferritic/ martensitic steel. The most notable feature of the results is that this BCC alloy shows a strain hardening behavior that is FCC like in character, even at low temperatures. In low dislocation density BCC single crystals dislocation, strain hardening and dislocation interaction mechanisms are dominated by the formation and collapse of junctions at the intersection of bowed edge segments of otherwise straight screw dislocations. In this regime, junction collapse is controlled by the rate of jog nucleation on the straight screw segments [8]. This suggests that strain hardening should be strongly dependent on both temperature and strain rate. However, such mechanisms are only dominant if the overall dislocation density is sufficiently low, and if edge segments are not effectively stored. This is clearly not the case in complex structural alloys, such as F82H, where nascent dislocation densities exceed $10^{14}/m^2$ [9] and complex pinning point and boundary structures result in complex mixed screw and edge substructures.

Kocks [5] rationalized Voce curves for FCC metals and alloys by developing a phenomenological model of strain-hardening, based on the storage and dynamic annihilation of dislocations and derived a linear relation between the strain-hardening and the flow stress similar to Equation 2. In Kocks' model, K_1 is the term related to the storage rate of dislocations, depending on their mean free path while K_2 characterizes the dynamic dislocation annihilation. It has been experimentally shown that dislocation annihilation takes place even at low temperatures in both FCC and BCC metals [10]. The annihilation of the screw segments can occur by cross-slip owing to the strong elastic interaction [11] between them and the annihilation of non-screw segments can take place either by climb (only important at high temperature) or by spontaneous annihilation when the attractive elastic force between two dislocations on different glide planes exceeds the force required for dislocation climb [12,13]. Note, in the Kocks model, the key structure parameter is is the total dislocation density; the detailed distribution of dislocations and their evolution with strain are not treated. Given the complex structure of these steels more detailed models

than that of Kocks should be evaluated. In particular, the evolution of the dislocation structure within the laths, the PAG and lath boundaries are likely to play important roles.

More advanced models have been developed to account for the evolution and reorganization of the dislocation structures up to large strain, e.g. [14-17]. For example, the recent cell structure-based (CSB) model of Fang and Dahl [16] yields a relation for the evolution of the dislocation density similar to that of Kocks by taking into account the reorganization of dislocations. They showed that Kocks' model is a simplification of their CSB model. In the context of their model, the physical significance of K_1 has to be related to the mean free path of the dislocation in the cell interior and in the trapping rate of mobile dislocations in the walls, while that of K_2 lumps together all the annihilation effects. The development of the microstructure as a function of strain, the influence of the size distribution of the carbides and the PAG size resulting from the initial heat treatment are a few examples of parameters whose influence on the flow stress and strain hardening needs to be investigated further.

Fracture toughness testing

As a part of an extensive study of the effect of specimen geometry and specimen size on fracture toughness, a series of fracture toughness tests were carried out on fatigue pre-cracked 0.18T compact tension (CT) specimens with a/W=0.5 and a specimen thickness (B) to width (W) ratio of B/W = 0.5. These are the same type of CT specimens which are also currently being irradiated in the Budapest Research Reactor as part of the MACE study. Thus the effective toughness, K_e, results reported here constitute a baseline for the unirradiated material. The typical brittle to ductile transition curve obtained in the lower shelf region is presented on Figure 12, where the typical and inherent large scatter is observed. All specimens failed by quasi-cleavage, in some cases after a large amount of plastic deformation and crack blunting, resulting in the so-called "loss of constraint". Constraint loss is primarily associated with plasticity encompassing a large fraction of the uncracked ligament of length, b. The degree of such in plane constraint loss can be generally characterized by a non-dimensional constraint parameter M as

$$M = b\sigma_y E / K_e^2$$

where E' is the plane strain elastic modulus. For this specimen geometry, values of M greater than about 75 are sufficient to ensure relatively high constraint. Thus in this case the maximum valid toughness that can be measured where $K_e \approx K_{Jc}$ is about 90 MPa√m. Below this value, contraint loss initially occurs gradually, with K_e increasing roughly as $M^{-1/4}$ [18]. At temperatures higher than 180K, a clear lateral contraction of the specimens near the crack tip was observed suggesting additional out-of-plane constraint loss. In this regime both in-plane (controlled by b) and out of plane (controlled by B and side grooving) constraint rapidly diminishes approaching plane stress conditions.

The effective fracture toughness data of the 0.18T CT specimens can be compared to previous results on precracked 20% sidegrooved 0.2T three point bend bars (3PB) [19], with a/W ≈ 0.5 and B/W = 1, shown as the open symbols in Figure 12. Clearly the effective toughness measured by the 3PB specimens is much lower than that found in the recent CT tests.

Figure 13 shows both sets of data corrected to small scale yielding (ssy) values based on three dimensional FEM calculations of Nevalaien and Dodds [20]. The correction is determined by calculating the large scale to small scale yielding ratio of the J/J_{ssy}, required to produce the same area within a specified non-dimensional principal stress (σ_p) contour normalized by the yield stress, $R = \sigma_p/\sigma_y$. The magnitude of the correction for a given M factor depends on the particular specimen geometry, alloy constitutive law and R. The small scale yielding estimates are given by $K_{Ic} \approx K_e/(J/J_{ssy})^{0.5}$. In this case R was taken as 3 and the strain-hardening exponent was assumed to be 0.1. The ssy values are similar, although the CT data still fall somewhat above those for the 3PB specimens.

While providing a reasonably consistent estimate of K_{Ic} from both specimen sets, the results do not fully explain the separation of the uncorrected data. There are several possible explanations including some combination of:

- Weakest link-type statistical effects associated with the crack front length which is roughly 2.8 larger for the 3PB compared to the CT specimens.
- The maintenance of greater lateral constraint for the 3PB specimens with W/B = 1.
- Details of the side grooving.
- Material inhomogeniety.

Unfortunately it is not possible to determine which, or which combination, of these effects may be responsible. Further testing and analysis is planned to clarify this issue.

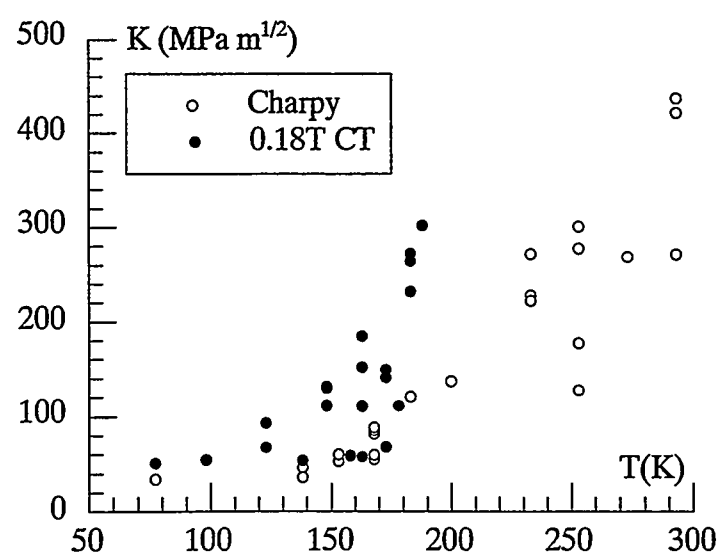

Figure 12: Fracture toughness measured with 0.18T CT and 3PB specimens

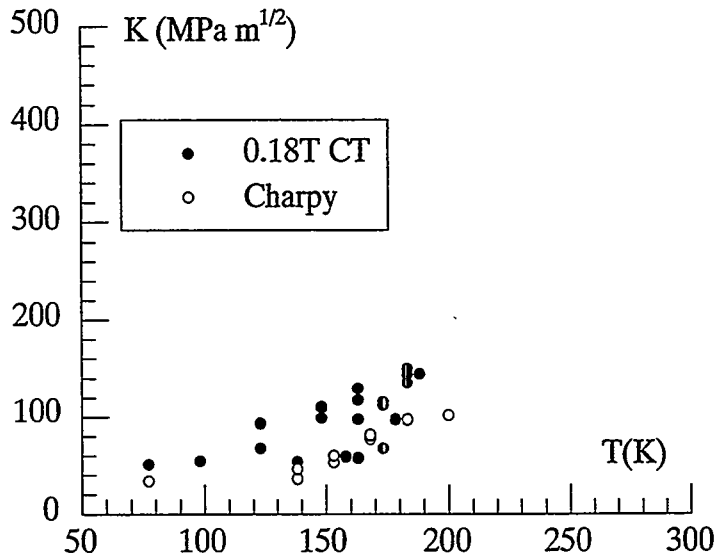

Figure 13: Constraint corrected fracture toughness measured with 0.18T CT and 3PB specimens

MACE status

The first irradiation of the IEA steel specimens started in April 1999 at the Budapest Research Reactor KFKI AEKI. The test matrix is described elswhere [21]. The initial irradiation was carried out at 250°C for 768 hours which is estimated to yield the target dose of 0.5 dpa. Dosimetry capsules are being analyzed to confirm the preliminary estimates and, if necessary the capsule will be re-inserted for a time needed to reach the target exposure. Following irradiation the capsule will be shipped to the PSI for testing in their hot cells. Two additional sets of specimens are now being prepared at UCSB for irradiation at 250°C to 1 dpa and at 350°C to 0.5 dpa.

REFERENCES

[1] P. Spätig, E. Donahue, G. R. Odette, G. E. Lucas, J. Nucl Mat., ICFRM9 Proceedings, in preparation.

[2] P. Spätig, G. R. Odette, G. E. Lucas, J. Nucl Mat. (1999) accepted.

[3] H. Mecking, "Work Hardening in Tension and Fatigue", Ed. A. W. Thompson, p. 67 Am. Inst. Min. Engrs, N.Y. (1977).

[4] E. Voce, J. Inst. Metals, 74 (1968) 537.

[5] U. F. Kocks, ASME J. Eng. Mater. Technol., 98 (1976) 72.

[6] K. Edsinger, PhD Thesis, University of California, Santa Barbara, 1995, p.115

[7] A. H. Cottrell, F. R. S. and R. J. Stokes, Proc. R. Soc. A 233, (1955) 17.

[8] M. Tang, B. Devincre, L. P. Kubin to appear in Model. Simul. Mater. Sci. Eng.

[9] R. Schäublin, P. Spätig, M. Victoria, J. Nucl. Mater. 258-263 (1998) 1178.

[10] U. Essmann, H. Mughrabi, Phil. Mag. A, 40 No 6 (1979) 731.

[11] U. Essmann, Acta Metall., 12 (1964) 1468.

[12] J. Friedel, "Dislocations", Ed. Pergamon Press, London, (1964).

[13] U. Essmann, M. Rapp, Acta Metall. 21 (1973) 1305.

[14] X. F. Fang, W. Dahl, Mater. Sci. Engng. A203 (1995) 14.

[15] X. F. Fang, C. O. Gusek, W. Dahl, Mater. Sci. Engng. A203 (1995) 26.

[16] X. F. Fang, W. Dahl, Mater. Sci. Engng. A203 (1995) 36.

[17] Y. Estrin, L. S. Tóth, A. Molinari, Y. Bréchet, Acta Met. 46 No 15 (1998) 5509.

[18] H. J. Rathnun, G. R. Odette, G. E. Lucas, M. Y. He, J. W. Sheckerd, Proceedings of ASME Pressure Vessels and Piping Conference, Boston 1999, to appear.

[19] G. R. Odette, K. Edsinger, G. E. Lucas, E. Donahue, Small Specimen Test Techniques, ASTM STP 1329, American Society for Testing and Materials (1998) p. 298

[20] M. Nevalainen, R. H. Dodds, Inter. J. Fracture, 74 (1995) 131.

[21] Odette, G.R., Lucas, G.E., Spatig, P., DOE/ER-0313/25, Department of Energy (1999) 119-124